Nanoscale

Accepted Manuscript

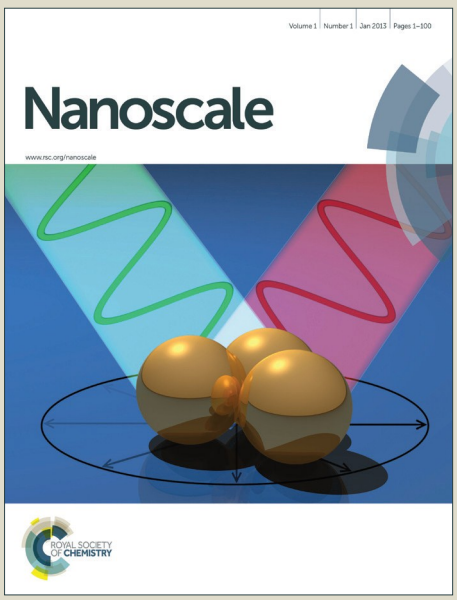

ROYAL SOCIETY OF CHEMISTRY

www.rsc.org/nanoscale

Rational design of DNA-actuated enzyme nanoreactors guided by single molecule analysis†

Soma Dhakal[1], Matthew R. Adendorff[2⊥], Minghui Liu[3,4⊥], Hao Yan[3,4,*], Mark Bathe[2,*], Nils G. Walter[1,*]

[1]Department of Chemistry, Single Molecule Analysis Group, University of Michigan, Ann Arbor, MI 48109, USA. [2]Department of Biological Engineering, Laboratory for Computational Biology & Biophysics, Massachusetts Institute of Technology, Cambridge, MA 02139, USA. [3]Center for Molecular Design and Biomimetics, The Biodesign Institute, [4]Department of Chemistry and Biochemistry, Arizona State University, Tempe, AZ 85287, USA.

⊥These authors contributed equally to this work.

*Corresponding authors: N. G. W. (nwalter@umich.edu); M. B. (mark.bathe@mit.edu); H. Y. (hao.yan@asu.edu)

†**Electronic supplementary information (ESI) available:** Details of the DNA sequences, assembly, and bulk characterization of all DNA tweezers; details of the smFRET characterization of the tweezers; additional AFM images; detailed results of MD simulation; bulk measurement of tweezer-scaffolded G6pDH activity; and single molecule measurements of tweezer-scaffolded G6pDH activity.

Abstract

The control of enzymatic reactions using nanoscale DNA devices offers a powerful application of DNA nanotechnology uniquely derived from actuation. However, previous characterization of enzymatic reaction rates using bulk biochemical assays reported suboptimal function of DNA devices such as tweezers. To gain mechanistic insight into this deficiency and to identify design rules to improve their function, here we exploit the synergy of single molecule imaging and computational modeling to characterize the three-dimensional structures and catalytic functions of DNA tweezer-actuated nanoreactors. Our analysis revealed two important deficiencies – incomplete closure upon actuation and conformational heterogeneity. Upon rational redesign of the Holliday junctions located at their hinge and arms, we found that the DNA tweezers could be more completely and uniformly closed. A novel single molecule enzyme assay was developed to demonstrate that our design improvements yield significant, independent enhancements in the fraction of active enzyme nanoreactors and their individual substrate turnover frequencies. The sequence-level design strategies explored here may aid more broadly in improving the performance of DNA-based nanodevices including biological and chemical sensors.

Table of Content (TOC) Figure

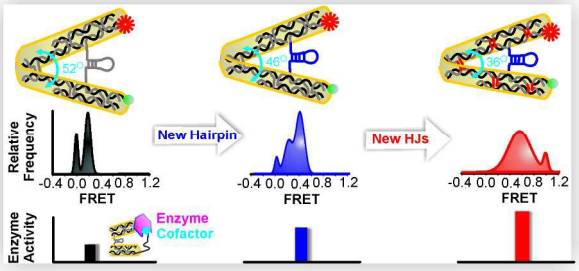

Using experimental and computational approaches to define sequence-level design principles that enable rationally improved closure and tweezer-actuated enzyme function of a DNA tweezer.

Introduction

Supramolecular DNA nanodevices driven by external signals such as strand displacement or environmental chemical cues enable actuation of nanoscale reactions with precise spatial control.[1-9] DNA tweezers are prototypical such nanomachines[10] that enable actuation in response to their environment for applications ranging from DNA-templated chemical coupling reactions,[11] pH-sensing to monitor cellular trafficking,[12] actuated protein capture,[13] and enzyme nanoreactors.[14] While these nanodevices have potentially broad utility, their performance is often found to be suboptimal when compared with idealized expectations. As a result, the performance of DNA nanodevices has been possible to improve by following empirical design rules such as the insertion of base pairs between crossovers,[15] fine-tuning of staple-strand break positions,[15] use of buffer additives,[16] and manipulation of the folding pathway.[17] However, the field of DNA nanotechnology is largely driven by the need for improved engineering rather than molecular understanding to inform device design. For example, while a glucose-6-phosphate dehydrogenase (G6pDH)/NAD^+ enzyme/cofactor pair at the ends of the two arms of the DNA tweezer-actuated enzyme nanoreactor can be activated and inhibited repeatedly, the relative enhancement between the two states was previously found to be under 6-fold.[14] In an effort to understand and resolve the basis of this relatively modest enhancement observed in bulk solution, we turned to single molecule imaging and analysis as a powerful means for studying nanoscale structure-function relationships in the underlying DNA tweezer.[18,19] In addition, we performed molecular dynamics (MD) simulations of single tweezers in large solvent boxes using periodic boundary conditions (PBC).

Although DNA nanodevices are mainly comprised of single and double crossover motifs composed of Holliday junctions (HJs), a systematic study of structure-function relationships is currently lacking. The DNA tweezer is archetypal in that its two arms are composed of each two HJs that are connected by a

single HJ hinge (Fig. 1a). Combining single molecule fluorescence resonance energy transfer (smFRET), MD simulations, and atomic force microscopy (AFM), we here have dissected the sequence-level origins of the sub-optimal performance of our DNA tweezer-actuated enzyme nanoreactors. Introducing a rational design strategy guided by smFRET and MD simulations, we improved tweezer closure and tweezer-actuated enzyme function by implementing modifications to both the hairpin actuator and architectural HJ elements. Most significantly, both smFRET and MD simulations show that the specific sequences of the HJs modulate the inter-arm distance (IAD) and conformational heterogeneity of the tweezer, which both can be reduced by a simple sequence redesign. We anticipate that our rational design strategies – empowered by the synergy of multiple techniques including smFRET, MD simulations, and AFM – provide general guidelines for improving other DNA nanodevices that will enhance their performance in future applications.

Results and Discussion

The original DNA tweezer[13,14] is composed of nine DNA oligonucleotides (Fig. 1a, Tables S1-S6[†] in ESI Section 1) that self-assemble to form two tweezer "arms" composed of double crossover (DX) motifs connected by a single immobile Holliday junction (HJ) 'hinge'. A single-stranded actuator element bridges the middle of the two arms and cycles between double-helix and hairpin conformations upon addition of fuel and antifuel strands that open and close the tweezer, respectively (Fig. 1a). To characterize tweezer actuation and quantify its closed-state conformation, we used smFRET to monitor surface-immobilized single tweezers by total internal reflection fluorescence microscopy (TIRFM) upon attachment of a Cy3 and Cy5 fluorophore pair to the ends of the tweezer arms via deoxy(d)T_3 and dT_4 tails, respectively (Fig. 1a, see Experimental and ESI Section 2 for smFRET experiments). The FRET pair was thus situated near the attachment sites of enzyme and cofactor to estimate their distance via the

FRET efficiency. The initial construct contained an actuator element with three-thymine (3T) spacers flanking each side of a 3-base pair (3bp) stem capped by a 13-nt loop[13,14] (Fig. 1a and S1†). While the opened-state showed a single, zero-FRET conformation (Fig. 1b), closure of the 3T3bp tweezer typically yielded two distinct FRET conformations of approximately 0 and 0.2, corresponding to inter-arm distances (IAD_{FRET}) of >10 and ~6.3 ± 0.2 nm (Fig. S7†, see Experimental for IAD estimation), respectively, that only slowly interconverted (Fig. 1c and S8†). The zero-FRET sub-population diminished upon increase in antifuel strand concentration, identifying it as tweezers remaining unclosed despite the presence of excess antifuel strand (Fig. S9†). AFM quantitatively supported the notion that the 3T3bp tweezer can be closed only to an IAD of ~6.3 nm (Experimental, Fig. S18† in ESI Section 3). To gain sequence-level insight into possible structural origins for the large IAD in the closed-state, we performed all-atom molecular dynamics (MD) simulation as described in Experimental and Section 4 in ESI of a model 3T3bp tweezer in solution under experimental conditions. The 13-nt closing loop of the hairpin actuator was excluded in all MD simulations due to its long equilibration time. However, we observed that the included hairpin stem remains fully formed throughout our simulations, indicating that excluding its closing loop does not make a significant difference in the IAD_{MD} observed. Results revealed that the tweezer arms splay in a three-dimensional manner that is facilitated by the long and flexible three-thymine spacers that bridge the actuating hairpin, resulting in a predicted mean IAD_{MD} of 5.3 nm (Fig. 1d, Movie SM1†). This structural origin of the observed incomplete closure offers a straightforward explanation for the limited bulk activity enhancement observed for an enzyme

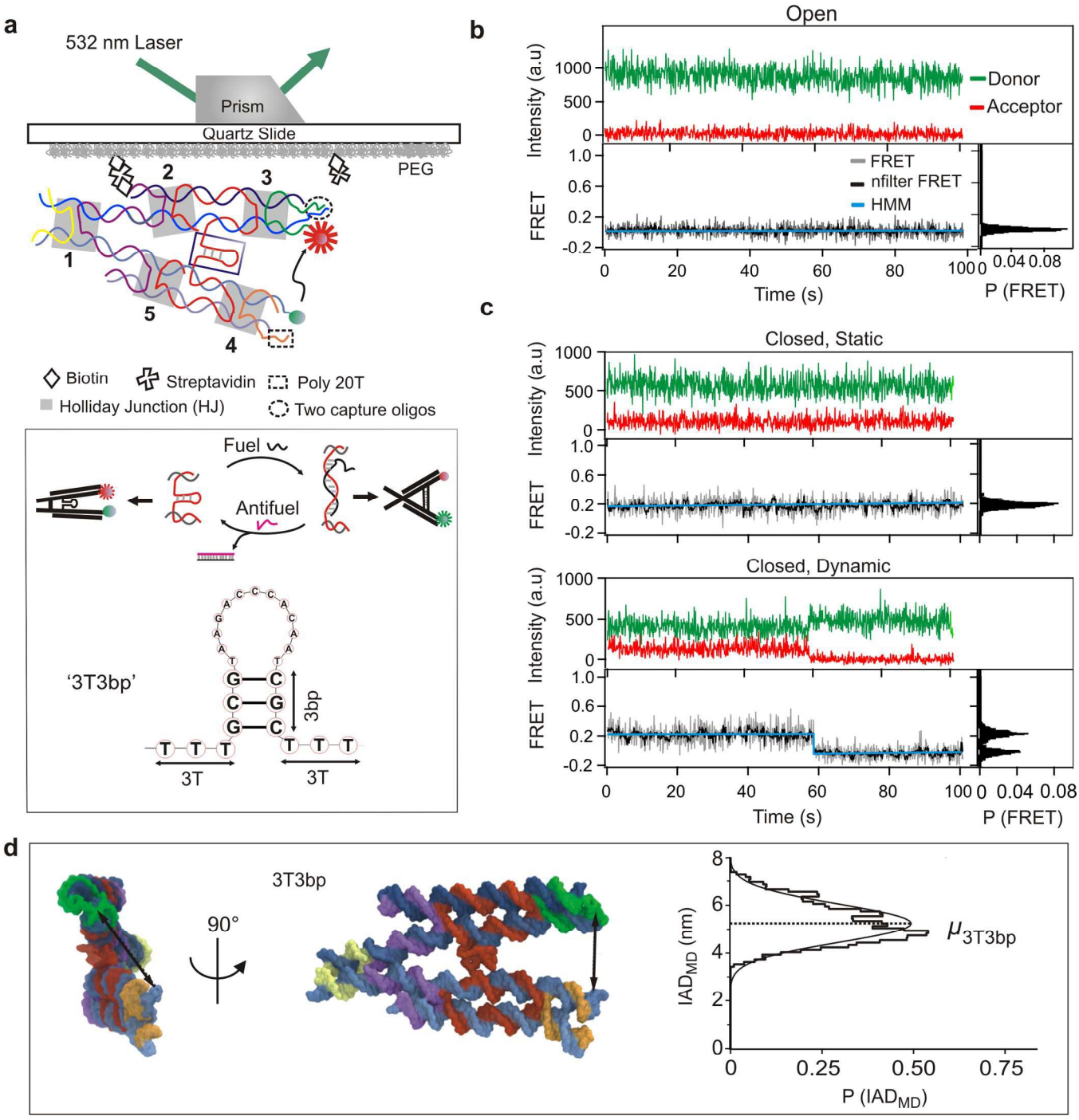

Fig. 1. Single molecule characterization of DNA tweezer conformation. (a) Experimental strategy for smFRET. Top panel depicts the surface immobilization of biotin-modified DNA tweezer on a PEG/streptavidin coated quartz slide. The hairpin actuator is boxed and other sturctureal elements are highlighted. The bottom panel depicts the opening and closing cycles of a DNA

tweezer actuated by fuel and antifuel strands, respectively. The sequence details of the hairpin actuator '3T3bp' in the bottom panel summarize our nomenclature of the tweezer used in this study. (b) Typical smFRET time traces for the opened-state tweezer. The overlaid black and cyan traces are nfilter and HMM idealized data, respectively. (c) Typical smFRET time traces for static (top panel, 72% molecules) and dynamic (bottom panel, 28% molecules) closed-state tweezers, determined by HMM analysis over 100 s total observation time. Only molecules with active FRET acceptor (confirmed at the end of each experiment by direct excitation with a 640-nm red laser) were used for analysis. The right-hand panels in b and c depict the corresponding FRET probability distributions for the molecules shown. Imaging was performed at 100 ms camera integration time. (d) Two representative orthogonal views of a typical molecular conformation from MD, corresponding to an IAD_{MD} of 5.3 nm (left), with the probability distribution of mean, μ_{3T3bp} (right). The IAD_{MD} of 5.3 nm is highlighted by double-sided arrows in the orthogonal views of the tweezer.

juxtaposed with its cofactor at the ends of the two arms of the nanoreactor[14] (Fig. S25†, S26† and Table S9†).

To force improved closure of the tweezer, we redesigned the 3T3bp architecture by eliminating the thymine spacers and hairpin entirely in a 0T0bp construct. While this redesign was anticipated to bring the tweezer arms into the closest possible proximity upon closure, smFRET characterization revealed even poorer closure (IAD_{FRET} = 6.8 ± 0.1 nm, Fig. S10a†) that MD simulations indicated is due to interarm twisting from crossover strain induced in this square-lattice design (IAD_{MD} = 4.7 nm, Fig. S21†, Movie SM2†). Similar results of DNA distortion in DNA nanodevices designed on a cubic lattice

that does not match the regular helical pitch of 10.5 bp/turn of B-form DNA have been observed in other contexts,[20,21] but to the best of our knowledge never at the single HJ level, as observed here.

To relieve this lattice strain we instead introduced single-thymine spacers intervening each tweezer arm of the actuating hairpin (Fig. S1†), which has previously been suggested to mitigate inter-duplex strain.[22,23] MD simulations (Figs. 2a, S21† and S22†, Movies SM2† and SM3†) suggested a hypothetical mechanism for improved closure that was consistent with smFRET measurements (Fig. S10b†) from a tweezer containing single-thymine spacers (1T0bp), which may have relieved the inter-arm distortion observed in the model of the 0T0bp construct. Experimental implementation using a 1T3bp tweezer redesign confirmed substantial improvement of the closed-state, as evidenced by 30% higher mean FRET (Fig. 2b). However, a significant low-FRET population in the closed-state remained together with conformational heterogeneity and slow interconversion dynamics (Fig. S11†). We interpret the observed slow FRET fluctuations as interconversion dynamics of the tweezer, rather than effects on the dye photophysics, since they varied with the tweezer design (discussed later; compare, for example, the FRET dynamics in Fig. S13† and S15†) without any obvious change in the local dye environment. Because DNA hairpins are known to exhibit heterogeneity in their conformational dynamics, next we tested whether ineffective closing and actuation of the tweezer could be improved by redesign of the actuating hairpin itself. In particular, we hypothesized that the 3bp duplex stem may be insufficient to retain the tweezer in the closed-state, so we extended it to a 4bp or 5bp stem to enhance its predicted thermodynamic stability (Fig. 2b, c and S1†). Both the 1T4bp and 1T5bp architectures indeed resulted in improved closure, manifest in shifts towards higher FRET populations in the closed-state that were well supported by AFM (Fig. 2b-d). However, the 1T5bp design exhibited considerably higher heterogeneity than the other constructs (Fig. S13†) and did not fully open upon fuel-strand addition (Fig. 2b),

presumably because the fuel-strand less efficiently competes with the thermodynamically most stable 5bp hairpin. Thus, the

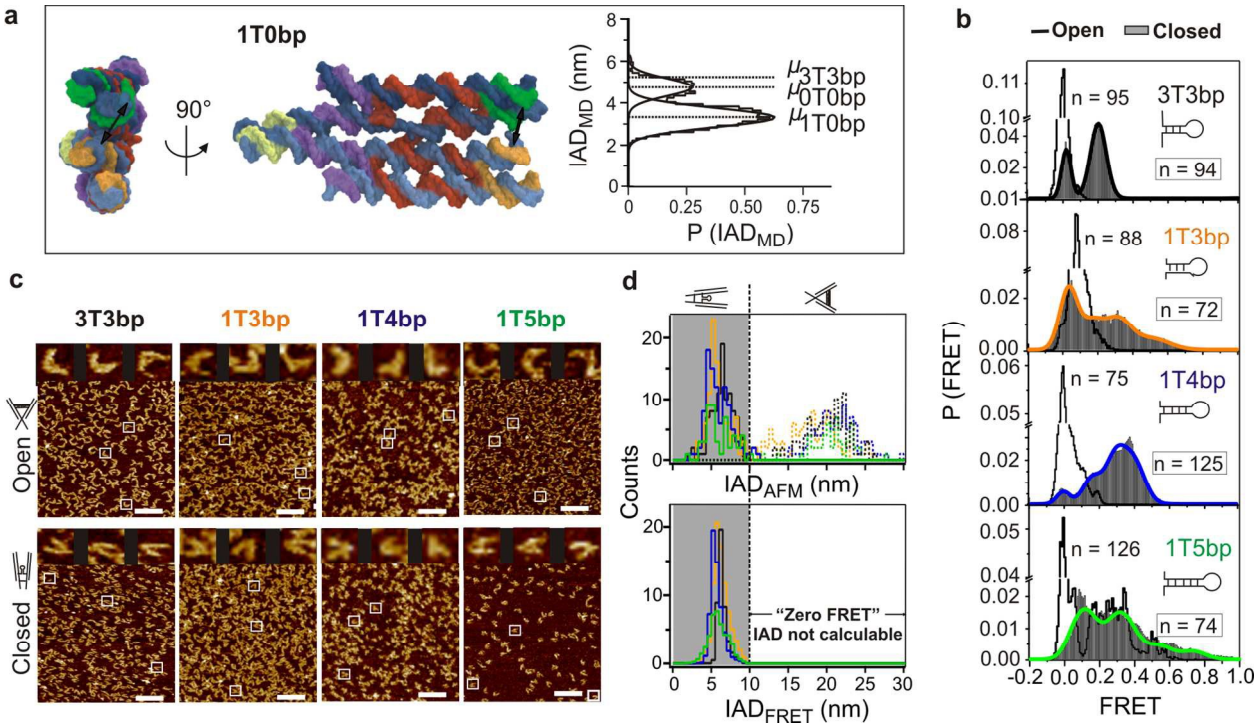

Fig. 2. Optimization of the hairpin actuator element improves tweezer closure. (a) Two orthogonal views of a typical conformation corresponding to the mean IAD_{MD} of 3.3 nm of the lower subpopulation (highlighted by black double-arrows) and the full IAD_{MD} distribution (right), predicted using MD of the tweezer with only a single-thymine spacer and no hairpin (1T0bp), showing a substantially reduced IAD_{MD} compared with the three-thymine spacer (3T3bp) and zero-thymine (0T0bp) spacer. (b) FRET probability distributions of closed-state and reopened tweezers containing different hairpin linkers—'3T3bp', '1T3bp', '1T4bp', and '1T5bp'. (c) AFM visualization of opened-state (top panel) and closed-state (bottom panel) tweezers. Scale bar is 100 nm. The zoom-in images of the tweezers (42 nm × 42 nm are shown) are placed in the same order as they (highlighted by boxes) appear from left to right in the field of view. Please see Fig. S18† and S19† in the for an expanded field of view. (d) IAD distributions of both closed-state (solid

lines) and opened-state (dotted lines) tweezers as measured from AFM images (IAD_{AFM}, top panel) and closed-state tweezers measured by smFRET (IAD_{FRET}, bottom panel). The gray background guides the eye for comparing IADs of closed tweezers measured by AFM and smFRET. The populations to the right of the dotted line represent opened-state tweezers observed by AFM (top panel), whereas the corresponding IAD_{FRET} is beyond the sensitivity of smFRET (and observed as zero-FRET; bottom panel).

1T4bp design was optimal amongst the set explored, although conformational heterogeneity was not eliminated by this actuator element (Fig. 2b and S12†).

Conformational heterogeneity and long-timescale interconversion dynamics have been characterzied previously for immobile HJs.[24] Specifically, single HJs were observed by smFRET to exhibit differential thermodynamic preference for their two distinct isomeric states, iso-I and iso-II, with slow interconversion rates that depend strongly on ionic conditions.[25,26] Indeed, smFRET of HJ1 isolated from our tweezer and fluorophore labeled to distinguish the isomers (Fig. 1a and S14†) showed a preference for adopting iso-II that would be detrimental to the desired closing of the tweezer arms (Fig. S14†). Immobile HJ sequences employed in structural DNA nanotechnology have previously been enumerated,[27] with the J1 sequence of Seeman and co-workers exhibiting a strong preference for the preferable iso-I conformation.[28] While numerous core sequences of HJs have been investigated conformationally in isolation,[25,26,29] as done here for HJ1 (Fig. S14†), the impact of these dynamics on higher-order programmed DNA assemblies composed of multiple such junctions have not been analyzed systematically. In fact, while the original tweezer design consisted of five immobile HJs (Fig. 1a), none were chosen to be the J1 sequence in its stable isomer. We therefore hypothesized that replacing the HJs

with the stable J1 junction designed to be in its preferred proximal iso-I state may further improve tweezer closing.

Because HJ1 serves as the tweezer hinge, we first redesigned it to be in the iso-I conformation, which significantly reduced the heterogeneity in the tweezer population (Fig. 3a). Subsequent redesign of all five HJs resulted in an additional substantial shift towards higher mean FRET (the IAD_{FRET} decreased to 4.4 ± 0.2 nm; Fig. 3a, S15† and S16†). As a negative control, we redesigned HJ1 to adopt its iso-II isomer, which resulted in a shift to a low-FRET region with increased conformational heterogeneity (Fig. 3a), as anticipated. We next imaged both the opened- and closed-state of the fully redesigned tweezer with AFM (Fig. 3b) and found that the mean IAD_{AFM} of the closed tweezers decreased to 4.1 ± 0.3 nm (Fig. S20†). MD simulation indicated that redesign of all five HJs resulted in a planar tweezer conformation that also brings the arms into closer proximity (Fig. 3c, S23† and S24†, Movies SM4† and SM5†). This flattening correlates with J_{twist} values for the junctions adopting distributions that are on average closer to zero (Fig. 3d). MD simulations additionally suggested that the dye-linked dT tails play an important role in stabilizing the high-FRET conformation via an inter-tail interaction across the arms (Fig. S24†). This interaction was enhanced in the construct with the redesigned HJs, suggesting cooperativity with flattening of the overall tweezer conformation. Addition of excess of dA_5 oligonucleotides in solution resulted in a shift towards lower FRET (Fig. S17†), consistent with this hypothetical inter-tail stabilization.

To investigate how the preceding architectural redesign improves catalytic function, we coupled the two arms of three representative tweezer designs – 3T3bp (original), 1T4bp (actuator-optimized), and 1T4bp-5HJs-iso-I (1T4bp with all five HJs redesigned to adopt iso-I) – with the enzyme G6pDH and its cofactor NAD^+ to generate DNA-tweezer actuated nanoreactors.[14] Utilizing a PMS/resazurin coupled reaction we monitored the G6pDH activity in bulk solution by fluorescence (Fig. 4a, ESI Section 5).

Compared to the original 3T3bp nanoreactor, 1T4bp enhanced the reaction rate by ~2-fold, whereas 1T4bp-5HJs-iso-I enhanced the rate by ~3-fold (Fig. 4b, Fig. S25† and S26†). To probe the mechanism

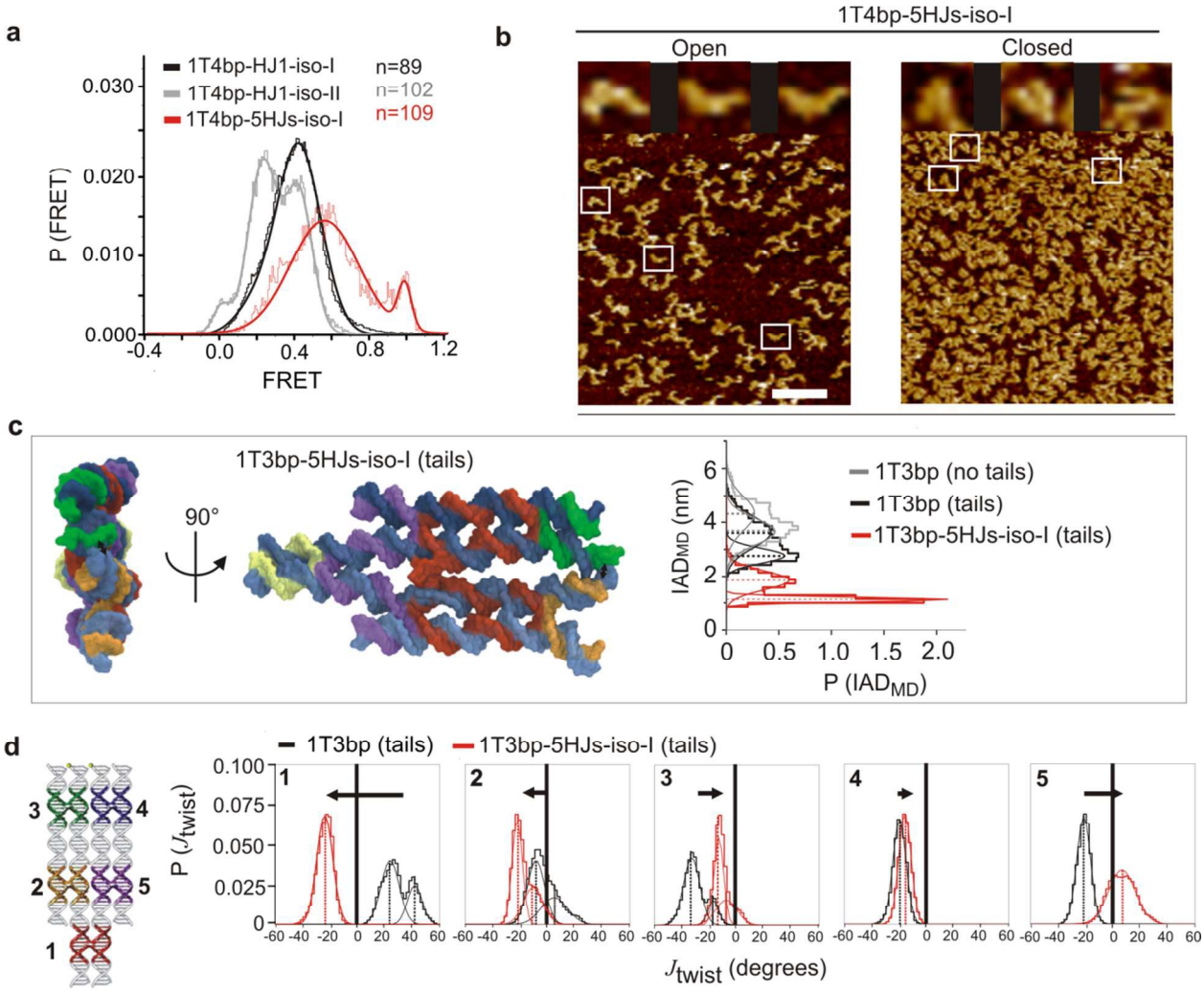

Fig. 3. Redesigned Holliday junctions improve tweezer closure. (a) FRET probability distribution of redesigned 1T4bp tweezers. The HJ hinge was redesigned to favor iso-I (1T4bp-HJ1-iso-I)), iso-II (1T4bp-HJ1-iso-II), or all five HJs were redesigned to favor iso-I (1T4bp-5HJs-iso-I). (b) AFM visualization of opened- and closed-state tweezers with all five HJs redesigned. Scale bar is 100 nm. The zoom-in images of the tweezers (42 nm × 42 nm are shown) are placed in the same order as they (highlighted by boxes) appear from left to right in the field of view. (c) Two orthogonal views of a typical conformation corresponding to the mean IAD_{MD} of 1.1 nm of the lower

subpopulation (highlighted by black double-arrows) of the '1T3bp-5HJs-iso-I' tweezer (left) and the corresponding IAD_{MD} distribution compared with the three earlier designs as indicated (right; dotted lines represent their means, μ). (d) Reduction in individual J_{twist} angles in tweezer 1T3bp-5HJs-iso-I (red) compared with the original junction design 1T3bp (black; dotted lines represent the means, μ, and solid, thick black lines highlight a J_{twist} angle of 0°, which correspond to the planar conformation). Compared with the original design, the mean J_{twist} angles of all but HJ2 are shifted (arrows) closer to 0° in the redesigned tweezer.

underlying these enhancements, we optimized our fluorescent assay to reach single molecule sensitivity when detected by TIRFM (Fig. S27† in ESI Section 6). Since the diffusion of resorufin is rather fast, 10% (w/v) PEG8000 in the imaging buffer (see Experimental for an estimation of the diffusion coefficient and elapsed time of resorufin) was used to detect single catalytic turnovers at 35 ms camera integration time in the form of single fluorescence spikes[30] (Fig. 4c and S27†). We note that due to the low concentration of resazurin (50 nM, Table S10†) used to avoid a high background, a slow turnover rate and low, easily detected spike frequency are expected (Fig. S27† and S28†). Compared to a control without substrate, the fluorescence spikes were noticeably more frequent (Fig. 4c). After applying an empirical intensity threshold to distinguish from noise (Fig. S27†), we found that only a subset (~20%) of 3T3bp nanoreactors were active (Fig. 4d). This observation is likely due to heterogeneity in enzyme orientation on the tweezer arm due to non-specific lysine-DNA conjugation. We note that controlling the enzyme orientation on the nanodevice is not trivial and will have to await future developments. In addition, due to the low concentration of resazurin used (50 nM, Table S10†) and our empirically informed intensity threshold to determine the fraction of active molecules, it is likely that we have

excluded some minimally active nanoreactors. However, our relative comparison of the fraction of active enzymes among different tweezer designs is independent of such technical limitations.

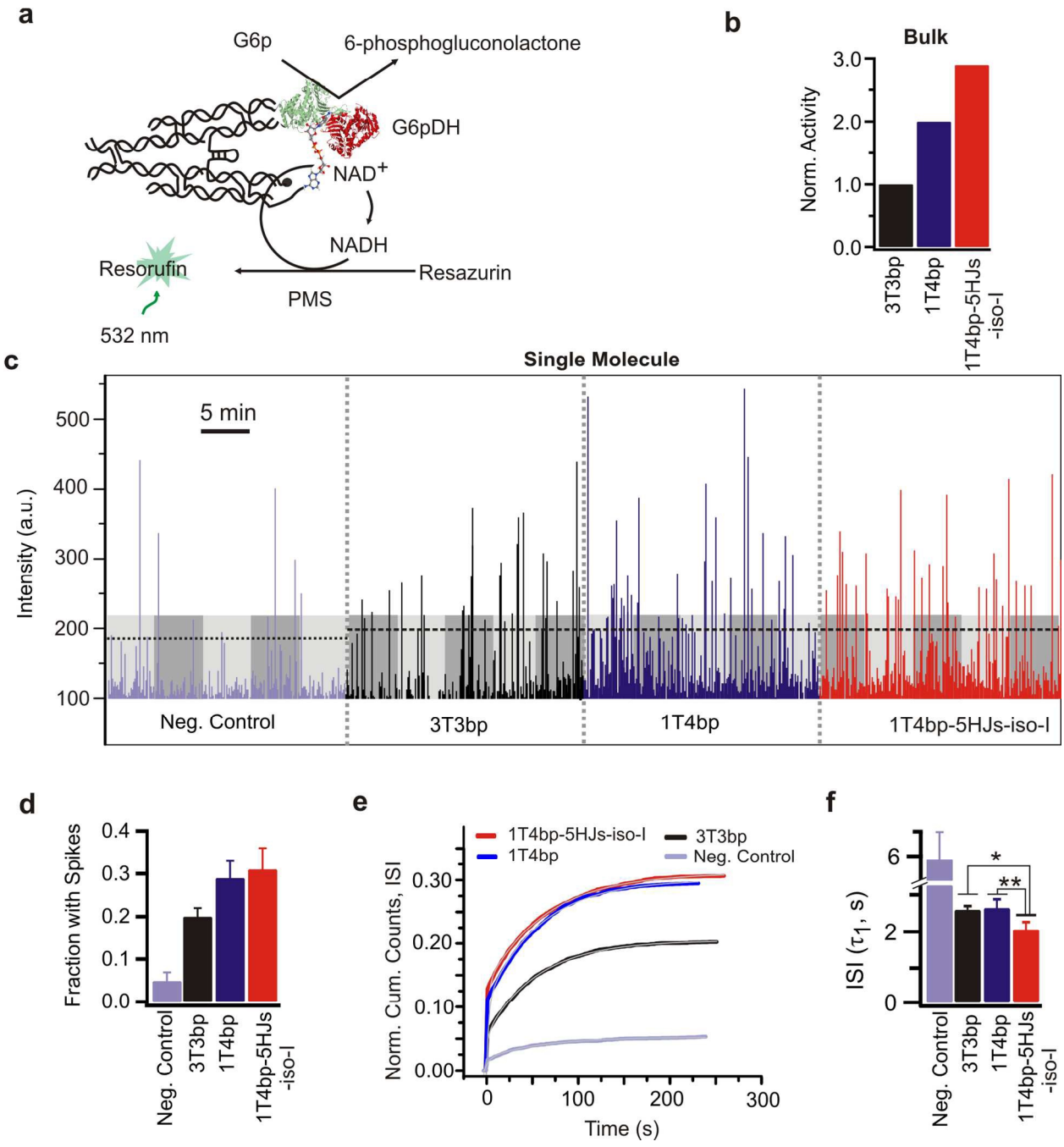

Fig. 4. Characterization of enzyme nanoreactor activity in bulk and at the single molecule level using a G6pDH/NAD$^+$ enzyme/cofactor pair. (a) Detection of enzyme activity is enabled by a

PMS/resazurin coupled assay in which the NAD^+ is reduced to NADH by G6pDH, followed by PMS-catalyzed electron transfer from NADH to resazurin to produce the fluorescent resorufin. (b) Relative bulk activity of the G6pDH/NAD^+-coupled original (3T3bp), linker-optimized (1T4bp), and junction-redesigned (1T4bp-5HJs-iso-I) tweezers. (c) Time traces for single nanoreactors with different tweezer designs. Each resorufin conversion leads to a single fluorescent spike. Five random 5-min-long traces from each tweezers were concatenated. The alternating gray and light-gray pattern highlights individual molecules in the concatenated traces. The horizontal dotted-lines represent an intensity threshold (chosen as mean + 8×standard deviation, SD). (d) Fraction of all enzyme nanoreactors of a particular tweezer design producing fluorescent spikes above the threshold (≥4 spikes above the dotted line in panel c). For the "Neg. Control" lacking G6p, an average from all three tweezer designs is reported. (e) Cumulative frequency of the inter-spike interval (ISI). These data are best fitted with double-exponential increase functions, yielding two time constants (τ_1 and τ_2). (f) Comparison of the short ISIs (τ_1) extracted from the plot in panel e, reflecting the most active enzyme sub-states. Please note that the negative control shows a ~2.5-fold longer ISI from spontaneously generated resorufin. The 1T4bp tweezers with all HJs redesigned (1T4bp-5HJs-iso-I) demonstrated the shortest ISI (*P < 0.05 and ** P < 0.05).

Accordingly, increasing numbers of nanoreactors became active with improved closure: 28% for 1T4bp and 32% for 1T4bp-5HJs-iso-I (Fig. 4d). The average spike frequency per molecule was similar (0.021 s^{-1}) for the 3T3bp and 1T4bp tweezers and increased to 0.024 s^{-1} for 1T4bp-5HJs-iso-I (Fig. S29†). We further discovered bursting among these spikes that we dissected by spike train analysis[31] (Fig. S29†), plotting the cumulative population distribution of inter-spike intervals (ISIs) for each tweezer design

normalized to the total fraction of active nanoreactors (Fig. 4e). These data were best fitted with double-exponentials, revealing (at least) two populations: one with a relatively short average ISI (τ_1), the other with a relatively longer average ISI (τ_2). In accord with previous single molecule studies of enzymes,[30,32,33] we interpret these two populations as distinct enzyme conformational sub-states. The population with short ISIs corresponds to enzymes in an optimal catalytic conformation (Fig. 4f), whereas the population of longer ISIs corresponds to enzymes in non-optimal, catalytically less active conformations (Fig. S30†). Strikingly, the mean short ISI (τ_1), or wait time between catalytic events of highly active enzymes, did not change from the 3T3bp to the 1T4bp tweezer, but decreased (from 2.7 ± 0.2 s for 1T4bp to 2.0 ± 0.2 s for 1T4bp-5HJs-iso-I) with the redesigned HJs of 1T4bp (Fig. 4f). Our single molecule observations thus suggest that we have discovered two independent mechanisms for improving nanoreactor performance: (i) a greater number of nanoreactors reach the critical IAD distance needed for activating their coupled enzyme with its cofactor due to improved closure upon optimized design of the actuator hairpin; and (ii) more frequent substrate turnover is achieved when stabilizing interarm tail-tail interactions are implemented that lead to straighter tweezer arms resulting from improved HJ sequence design.

Experimental

Materials

Enzyme. Glucose-6-phosphate dehydrogenase (G6pDH, *Leuconostoc mesenteroides*) was purchased from Sigma (St. Louis, MO, USA).

DNA oligonucleotides. All modified and unmodified DNA oligonucleotides were ordered from Integrated DNA technologies (IDT, Coralville, IA, USA). Cy3- and Cy5-labeled oligonucleotides were HPLC-purified by the manufacturer.

Crosslinking reagents. *N*-Succinimidyl 3-(2-pyridyldithio)-propionate (SPDP) was ordered from Pierce. Disuccinimidyl suberate (DSS), N,N-Diisopropylethylamine (DIPEA), and Dimethyl sulfoxide (DMSO) were purchased from Sigma.

NAD^+. β-Nicotinamide-N6-(2-aminoethyl) adenine dinucleotide (6AE-NAD^+ or AE-NAD^+) was ordered from BIOLOG (Bremen, Germany). Unmodified NAD^+ was ordered from Sigma.

***Substrates and activity assay reagents*:** Glucose-6-phosphate (G6p), resazurin (RESA), and phenazine methosulfate (PMS) were purchased from Sigma.

Design, assembly, and bulk characterization of DNA tweezers

DNA tweezer design. The detailed sequences of the DNA tweezers are shown in Tables S1-S5[†]. The computer program of Tiamat (http://yanlab.asu.edu/Resources.html) was used to facilitate the structure design. The design is based on one previously described[14] except that TB1 is labeled with biotin at 3' end.

Denaturing PAGE purification of oligonucleotides. Oligonucleotides purchased from IDT were purified using the same method as described.[34]

DNA tweezer assembly. The DNA strands constituting each DNA structure were mixed in 1×TAE-Mg^{2+} buffer (40 mM Tris, 20 mM acetic acid, 2 mM EDTA and 12.5 mM magnesium acetate, pH 8.0) to reach a final concentration of 0.5 μM per strand, except for the NAD^+-conjugated DNA strands, which were added to the mixture at a final concentration of 0.75 μM, and the fuel strands, which were added at

a final concentration of 1 μM. All samples were annealed in an Eppendorf Mastercycler using an annealing protocol as described.[14] The formation of the DNA structures was characterized by native polyacrylamide gel electrophoresis (PAGE). For single molecule measurements, tweezer samples were further purified by running a 5% native PAGE for 2 h at a constant voltage of 200 V; the major bands representing assembled DNA tweezers were visualized by UV-shadowing and cut from the gel, chopped into small pieces, and incubated for 1 h in 1×TAE-Mg^{2+} buffer. The DNA nanostructures were extracted from the gel pieces by centrifugation at 8,000 rpm for 10 min using a Costar Spin X filtration device (Corning, cellulose acetate membrane with 0.22 μm size). DNA nanostructures were collected in 1×TAE-Mg^{2+} buffer and concentrations were measured by UV absorbance at 260 nm using the extinction coefficient (Table S6†) estimated by the IDT Biophysics analyzer (http://biophysics.idtdna.com/UVSpectrum.html). Samples for bulk measurements were assembled with regular T3 and TP8 strands without fluorescent dyes. Samples for single molecule measurements were assembled with Cy3/ Cy5- labeled strands.

Isolated Holliday junction (HJ) assembly. The isolated Holliday junction "hinge" (HJ1) was assembled similarly to the DNA tweezers. The detailed sequence is provided in Table S5†. The T5 strand was modified with biotin to enable surface capture for single molecule experiments. In Labeling Scheme-I, the T3 and T6 strands were modified with Cy3 and Cy5, respectively. In Labeling Scheme-II, the TP2 and T6 strands were modified with Cy3 and Cy5, respectively.

Preparation, purification, and characterization of protein-DNA conjugates. Preparation, SPDP crosslinking conjugation, FPLC purification and characterization steps of protein-DNA conjugates were the same as described.[34] The protocol was optimized to purify protein with two conjugated DNA oligonucleotides. Briefly, SPDP conjugation chemistry was used to crosslink G6pDH with a 5'thiol-modified DNA oligonucleotide (5'-HS-TTTTTCCCTCCCTCC). To allow amine-reactive N-

hydroxysuccinimide (NHS) esters to react with the lysine residues on the G6pDH surface, a 500 μL of 40 μM G6pDH was first reacted with a 2-fold excess of SPDP in 10 mM sodium HEPES (pH 8-8.5) for one hour. Excess SPDP was removed by washing, and purified using Amicon filters (30 kD cutoff). The SPDP-modified G6pDH was conjugated to a 7-fold excess of thiol-modified oligonucleotide through a disulfide bond exchange of the activated pyridyldithiol group. The reaction mixture was incubated in 10 mM sodium HEPES (pH 8-8.5) for one hour. The coupling efficiency was evaluated by monitoring the increase in absorbance at 343 nm due to the release of pyridine-2 thione (extinction coefficient: 8080 M^{-1} cm^{-1}). A homogeneous mixture of G6pDH-DNA conjugate with an average labeling ratio of ~2 DNA oligonucleotides per G6pDH was purified by anion exchange chromatography using AKTA fast-protein liquid chromatography (FPLC, GE Healthcare) as described.[34]

Preparation, purification and characterization of NAD^+-DNA conjugates. The method for the conjugation and HPLC purification was similar to that reported in previous publications.[14,34]

Protein-DNA tweezer assembly and purification. As described in a previous publication,[14] a 3-fold molar excess of oligonucleotide-conjugated G6pDH was added to the pre-annealed tweezer structures and mixed well. Proteins were assembled by using a 1-h annealing protocol: the temperature was decreased from 37 ℃ to 10 ℃ and held at 4 ℃ using the established protocol.[14] Excess G6pDH-oligonucleotide was removed using monomeric avidin resin (Pierce) and biotin-labeled tweezers; the protein was eluted with 2 mM biotin at a recovery yield of ~30%.

Native gel characterization of the purified assembly. 3% non-denaturing PAGE was performed at room temperature over 2-2.5 h at a constant voltage of 200 V, and the gel subsequently stained with ethidium

bromide. The purified protein-DNA tweezers were quantified by absorbance at 260 nm and concentrations were calculated with estimated extinction coefficients (Table S6[†]).

Single molecule FRET (smFRET) characterization of DNA tweezers

Preparation of tweezers for smFRET. DNA tweezers containing Cy3 and Cy5 fluorophores on separate arms were prepared to monitor the opening and closing by smFRET. The tweezer was biotinylated on the TB1 strand to allow immobilization on streptavidin-coated microscope slides for single molecule study. Please see above for the tweezer assembly protocol.

Preparation of microscope slides and execution of smFRET experiments. PEGylated quartz slides were prepared using previously published procedures.[35] Briefly, the slides were reacted with aminopropyltriethoxysilane (APTES) in acetone for 30 min to generate an amino-functionalized surface followed by a 3-h reaction with a 10:1 mixture of succinimidyl ester–functionalized O-methyl-PEG and biotin-PEG. The remaining unreacted amines on the quartz slides were removed by adding sulfo-disuccinimidyl tartrate for 30 min. A single flow-channel per slide was assembled using double-sided sticky tape and a glass coverslip. We added a solution of 0.2 mg ml^{-1} streptavidin in 1×T50 buffer (50 mM Tris-HCl, pH 7.5, 50 mM NaCl) to the channel and incubated for ~3 min at room temperature to capture DNA tweezers via the biotin/streptavidin interaction.

smFRET analysis. Unless otherwise noted, the doubly labeled DNA tweezers (~5 nM) were incubated with ~0.5-1 μM antifuel or fuel strand in 5 μL 1×TAE-Mg^{2+} buffer for ~5 min at room temperature to close/reopen the tweezer. The sample was further diluted to a concentration of 20-100 pM in imaging buffer (1×TAE-Mg^{2+}), flowed into the channel and incubated for 2-3 min. Excess tweezer and fuel/antifuel strands were removed by flowing 300-400 μL imaging buffer through the channel. For the

polyA experiment, the FRET movie of the closed tweezer was recorded with 1 μM polyA oligonucleotide added to the imaging buffer. The imaging buffer containing oxygen scavenger system (OSS) composed of 50 nM protocatechuate dioxygenase (PCD, Sigma), 5 mM protocatechuate (PCA, Sigma) and 2 mM Trolox (Acros) to retard photobleaching.[34] In the total internal reflection microscope (TIRFM), Cy3 was directly excited using a 532 nm laser (CrystaLaser CL532-050-L, 50 mW), and emission from Cy3 and Cy5 fluorophores was simultaneously recorded using an intensified CCD camera (iPentamax, Princeton Instruments) at 100 ms time resolution. The presence of an active FRET acceptor was confirmed at the end of each experiment by the excitation with a 640-nm red laser (Coherent CUBE 635-25C, 25 mW) as described.[34] The smFRET analysis of isolated Holliday junction was performed similarly except that a smaller field of view (80 × 256 pixels) was imaged to achieve 16 ms time resolution.

Fig. S6[†] shows representative fields of view from the smFRET experiments of different tweezers. smFRET time traces were extracted from the raw movie files using custom-written IDL (Research Systems) and analyzed using Matlab (The Math Works) scripts, as previously described.[34] The smFRET trajectories were screened for subsequent analysis based on the following expected features[34]: (1) single-step photobleaching; (2) total fluorescence of Cy3 and Cy5 exceeding 300 counts/frame; and (3) evidence of both Cy3 and Cy5 signal. A FRET value was calculated as $I_A/(I_A+I_D)$, where I_A and I_D represent the background corrected fluorescence intensities of the acceptor (Cy5) and donor (Cy3) fluorophores, respectively.[35]

The raw fluorescence intensity traces were processed using a non-linear filtering program adapted from published approaches.[36,37] Such nfilter analysis is useful to resolve underlying populations in broadly distributed FRET data that may otherwise be masked by noise. A set of casual and anti-casual predictors [2 4 6 8] running forward and backward in time, respectively, were used to smooth the donor and

acceptor traces. A window size (*M*) of 20 was used for the analysis.[36] Smoothed FRET traces were then calculated from smoothed donor and acceptor intensities as described above. FRET histograms were constructed from the first 1,000 frames of the nfiltered data of each molecule. The mean FRET values were obtained by Gaussian fitting of the FRET histogram.

Hidden Markov Modeling (HMM) of smFRET traces was performed for the first 100 s observation time as described.[35] We used a two-state model for all tweezers except for 1T5bp (due to its inter-conversion to three FRET states, a three-state model was used instead) to idealize the FRET data. Transition Occupancy Density Plots (TODPs) were then obtained from the idealized data using custom written Matlab scripts.[35] The HMM analysis was also used to count static/dynamic molecules.

For estimation of IAD from smFRET data (IAD_{FRET}), please see 'Inter-arm distance (IAD) estimations' below.

Atomic force microscopy (AFM) imaging of DNA tweezers

AFM imaging protocol. 2 μL samples were deposited onto a freshly cleaved mica surface (Ted Pella, Inc.) and left to adsorb for 2 min. 50 μL of 1× TAE-Mg^{2+} buffer was added to the sample, followed by 0.5 μL 100 mM Ni^{2+} to enhance DNA adsorption onto the mica. The samples were scanned using a SCANASYST-FLUID^{+} probe (Bruker, Inc.) in "Scanasyst in fluid" mode on a Multimode 5 AFM with Nanoscope V controller (Bruker Corporation). All AFM imaging was performed in solution at room temperature. For estimation of IAD from AFM images (IAD_{AFM}), please see 'Inter-arm distance (IAD) estimations' below.

Molecular dynamics (MD) simulations of DNA tweezers

Preparation of all-atom tweezer models. The sequence topology of the tweezer base-plate, comprising all bps not in the hairpin or dye linker motifs, was defined using the software caDNAno.[38] The three-dimensional mechanical ground-state conformation was subsequently calculated and atomic structure generated using the finite element based modeling framework CanDo[39,40] assuming anti-parallel Holliday junctions (HJ)[12]. DNA duplexes were assumed to have geometrical and mechanical properties consistent with B-form DNA. Axial rise per bp was equal to 0.34 nm, duplex diameter 1.85 nm in order to ensure crossovers were consistent with known HJ atomic structure[13], and 10.5 bp/turn was assumed. The axial stretching, bending, and torsional stiffnesses were assumed to be equal to 1100 pN, 230 $pNnm^2$ and 460 $pNnm^2$, respectively.[39] The all-atom PDB file generated using the atomic structure generation option in CanDo[41] was subsequently ionized and solvated in preparation for molecular dynamics. Thymine linkers, when present, were added by extending the pertinent strands using DS Visualizer's Macromolecules Toolkit.[42] Details of the modifications to attach the different hairpin motifs are described in ESI Section 4. The all-atom system was immersed in TIP3P[43] water and explicit Mg^{2+} and Cl^- ions were added to neutralize DNA charges and set the simulation cell Mg^{2+} ion concentration to 12.5 mM, consistent with experimental conditions.

Explicit solvent MD. All simulations were performed using the program NAMD2[44] with CHARMM27 force field[45,46] and Allnér Mg^{2+} parameters[47] with an integration time step of 2 fs and periodic boundary conditions (PBC) applied in an orthogonal simulation cell. The boundaries of the periodic water boxes used for all simulations were constructed to be three cut-offs away from the solute (tweezer construct) in both the X and Z directions, where Y runs along the long axis of the construct. In the case of the Y direction, the boundaries were set to be 1.5 cut-offs from the solute atoms on both sides of the box. With this periodic setup, the tweezer constructs do not interact with their mirror images across the boundaries, even at their maximum deformations. Van der Waals energies were calculated using a 1.2 nm cut-off

with a switching function applied from 1.0 to 1.2 nm. The Particle Mesh Ewald (PME) method[48] was used to calculate full electrostatics with a minimum grid point density of one per 0.1 nm. Full electrostatic forces were computed every two time steps (equal to 4 fs) and non-bonded forces were calculated at each time step (2 fs). Simulations were performed in the NpT ensemble using the Nosé-Hoover Langevin piston method[49,50] for pressure control with an oscillation period of 200 fs and a damping time of 100 fs. Langevin forces[51] were applied to all heavy atoms for temperature control (300 K) with coupling coefficients of five per picosecond. All hydrogens were constrained to their equilibrium lengths during the simulation and system configurations were recorded every 1 ps for downstream analysis of coordinates. Energy minimization was always performed on the orthogonal simulation cell prior to dynamics using the conjugate-gradient and line minimizer implemented in NAMD2, first on the solvent and ions alone for 10,000 steps with all nucleic acid atoms spatially constrained, followed by an additional 10,000 steps with all atoms unconstrained. All parameters for the minimization were identical to those used for dynamics. The system was then slowly heated (1 K per 10 ps) to 300 K and the pressure was allowed to equilibrate to 1 atm prior to production run MD.

Atomic distance calculations. The distance metric used to monitor temporal tweezer arm fluctuations ($IAD_{MD,}$ see 'Inter-arm distance (IAD) estimations' below for further details) is defined as the distance between the O5' atoms of the 5' end bases of the duplex segments of the T3 and T8 strands. Distances were calculated using the ProDy[52] suite of trajectory analysis functions. A Gaussian Mixture Model (GMM) was used to fit Gaussian distributions to each subpopulation in the data and the Bayesian Information Criterion (BIC)[53] was used to select the best-fitting number of Gaussians.

Calculation of HJ J_{twist} values from MD simulations. Inter-duplex crossing angles, J_{twist},[54] corresponding to the five in-plane scissor motions of each HJ were calculated at each trajectory frame for each tweezer. For each junction, the duplex arms were defined using the five bps flanking the strand

crossover site on either side of the junction, for a total duplex arm length of 10 bps. Local base-pair reference frames were fit to every bp of each arm using the program Curves+[55] to generate a helical axis for each arm. Two linear axis vectors were then generated by fitting a three-dimensional vector through the helical axis nodes. The dihedral angle between the resulting two linear vectors was used to define J_{twist}, where a positive value denotes a right-handed conformation and a negative value denotes a left-handed conformation. A GMM and the BIC were again used to fit multiple Gaussians to the subpopulations in the angle distributions from simulation.

Inter-arm distance (IAD) estimations

smFRET, AFM and MD each lead to slightly distinct estimates of the IAD due to the inherent differences in the nature of the underlying data (see our description below). Our aim was to make the IADs as comparable with one another as possible, by calculating them as follows. Nevertheless, a small variation (~0.5-1 nm) of the estimated IAD is expected between three different datasets.

IAD from smFRET (IAD_{FRET}). The IAD_{FRET} (equivalent to the inter-dye distance, R) and the apparent FRET efficiency, E_{app}, were calculated as described[56,57] from the equations:

$E_{app} = c[1+(R/R_0)^6]^{-1}$, where c = 0.69, R_0 = 54 Å, and $E_{app} = \dfrac{I_{Cy5}}{I_{Cy5} + I_{Cy3} \times \dfrac{(\phi_{Cy5} \times \eta_{Cy5})}{(\phi_{Cy3} \times \eta_{Cy3})}}$

φ and η signify the fluorophores quantum yields and detector channel efficiencies,[53,54] respectively. The donor and acceptor intensities I_{Cy3} and I_{Cy5}, respectively, were corrected for leakage of 20% of donor photons into the acceptor channel. Since we compared FRET values among different tweezer designs without altering local environment of the dyes, use of a literature value of R_0 is justified.

IAD from AFM (IAD_{AFM}). AFM images were analyzed with Veeco NanoScope Analysis software 1.20 (Build R1Sr3.64571). Original images were first flattened to fit each line individually to center data (0th order), remove tilt (1st order) and remove bow (2nd, 3rd order). The Measure tool built in Image Window was utilized to manually analyze the $IAD_{\mathbf{AFM}}$ between the inner ends of two arms. Smaller view areas were zoomed in with Data Zoom tool and moved to all scanning areas with the Pan tool.

The conformational sub-states of the closed tweezers observed by smFRET (Fig. 2b) were not very obvious in the IAD_{AFM} histograms (Fig. 2d and S20†). This is probably due to surface perturbation of the tweezer conformation due to the tight mica interaction. However, for a given tweezer, the overall distribution of IAD_{AFM} and IAD_{FRET} were comparable when the distances were binned equally to 0.5 nm (Fig. 2d).

IAD from MD simulation (IAD_{MD}). The IAD in MD simulation was defined as the distance between the O5' atoms of the 5' end bases on the T3 and T8 strands. The $IAD_{\mathbf{MD}}$ for each sub-population in a given construct was again determined using GMM and BIC fitting.

In general, we observed shorter a IAD_{MD} of tweezers compared to IAD_{FRET} and IAD_{AFM}, which may be due to the short timescales simulated (~100-200 ns) compared with the smFRET acquisition time (~100 ms), or the presence of poly-thymine tails to tether dyes to the tweezer arms. Notwithstanding, the relative pattern of the IADs among the different tweezers is in agreement with trends observed experimentally.

Bulk measurement of tweezer-scaffolded G6pDH activity

Bulk enzyme activity was measured for both opened- and closed-state tweezers. 100 nM DNA tweezers assembled with G6pDH/NAD^+ were assayed with 100 µL of 1mM glucose-6-phosphate, 1 mM phenazine methosulfate and 500 µM resazurin in 1 × Tris-buffered saline (TBS) buffer (50 mM Tris-HCl, pH 7.5, 150 mM NaCl) with no magnesium ions added. The same batch of protein-DNA and NAD^+-DNA conjugates was used to adequately compare the catalytic function among the different tweezer designs. The activity was measured by monitoring the fluorescence increase at 590 nm as described[14] and reported in Table S9†. The native gel characterization is shown in Fig. S4†.

Single molecule measurement of tweezer-scaffolded G6pDH activity

Using microscope slides with fluorescent beads as fiduciary markers. For the single molecule enzyme assay, streptavidin modified PEG slides (prepared as described above) were incubated for ~2 min with neutravidin coated fluorescent beads (FluoSpheres, specifications: 0.04 µm, excitation/emission; 550/605, 1% solids, Invitrogen) at a 1:1 million dilution in 1×T50 buffer, after which excess was flushed away with 400 µL of the same buffer. These fluorescent beads (~5-8 per field of view) were used as fiduciary markers (Fig. S27†) to correct for stage/slide drift over time. DNA tweezers carrying the enzyme/cofactor pair at the ends of the arms was injected for surface binding and a FRET movie recorded as described above. During analysis of each movie, the photobleaching donor (Cy3) channel of the initial movie was mapped based on a custom-written MATLAB script to the subsequent enzyme assay movie using the fiduciary beads as reference. This approach allowed us to keep track the locations (x- and y-coordinates) of all individual tweezers in a field of view even after photobleaching the FRET fluorophores, to follow the enzyme turnover over time at the predefined tweezer locations.

Imaging single enzyme activity. To measure the activity of tweezer-scaffolded G6pDH, the enzyme assay was performed on the same field of view after photobleaching the fluorophores. A substrate

solution was prepared in 1×TBS buffer (pH 7.5) containing 1 mM Mg^{2+} and 10% (w/v) PEG 8000 (Table S10†). The movie was recorded (35 ms camera acquisition time) immediately after injecting a substrate solution that lacked one of the substrates, glucose-6-phosphate (G6p). To compare the spiking behavior on the same field of view, a complete substrate solution was injected and a movie was subsequently recorded for ~5 min (9,091 frames) using TIRFM. In this single molecule assay, the activity of individual enzymes is observed as fluorescent spikes in the fluorescence-time traces due to formation of fluorescent resorufin through a catalytic cascade reaction (Fig. S27†). Fluorescence fluctuations over time were analyzed using a custom-written MATLAB script. The script allowed us to measure the background intensity of single molecule traces and set an intensity threshold to subtract from the raw traces. We used a high threshold (mean + 8×standard deviation, SD) to minimize the chance of detecting a freely diffusing resorufin molecule. Since we typically observed 1-3 spikes above this cut-off intensity in the control experiments ((-)G6p), probably due to non-specific (perhaps photoinduced) formation of resorufin, only molecules with ≥4 spikes were counted as active enzymes and considered for subsequent spike train analysis. Note that a low frequency of fluorescent spikes is expected due to our low concentration of substrate (50 nM resazurin, Table S10†), used to maintain a low background.

Estimation of diffusion constant and elapsed time of resorufin in 10% (w/v) PEG 8000. The diffusion coefficient of resorufin in the imaging buffer containing 10% (w/v) PEG 8000 is estimated using the Stokes-Einstein Equation:

$$D = \frac{k_B T}{6\pi\eta r}$$

Where the Boltzmann constant k_B = 1.3806488 × 10^{-23} m^2·kg/s^2·K; absolute temperature T = 298 K; viscosity of 10% (w/v) PEG 8000 η = 0.0089 kg/m·s;[58] and molecular radius r= 0.3×10^{-9} m.[59] Using these parameters, the diffusion coefficient D is estimated to be 8.18 × 10^{-11} m^2/s.

The elapsed time of the resorufin diffusion (t) is estimated using the following equation:

$$t = \frac{x^2}{2D}$$

Using the mean distance traveled x = 300 nm (the upper bound of TIRF detection distance from the surface), it takes approximately 0.6 ms for a resorufin molecule to diffuse out of the probe volume. However, this calculation is a lower estimate of the elapsed time because the molecular radius was used instead of the hydrodynamic radius, and the influence of other reagents on viscosity such as glucose-6-phosphate (G6p), resazurin and Mg^{2+} was not considered in the calculation for the sake of simplicity. This dwell time suffices to render the fluorescence signal detectable. By contrast, the diffusion coefficient of resorufin in water (η = 0.00089 kg/m·s [60]) at 298 K is 8.74 × 10^{-10} m^2/s and the corresponding elapsed time is 0.06 ms. This calculation suggests that the use of 10% (w/v) PEG 8000 slows down the diffusion of resorufin by at least 10-fold, critical for its single molecule detection.

Relating spike intensity and catalytic turnover. To identify the relationship between individual fluorescence spikes and the catalytic turnover number, we monitored the spike intensity and fraction of molecules with fluorescence spikes over a wide range of resazurin concentrations (0.5—100 nM, Fig. S28†). Fluorescence intensity time traces were recorded on TIRF microscope as described above except for the following changes. The Cy3 labeled DNA modified G6pDH molecules (G6pDH-(5'-TTTTTCCCTCCCTCC)-Cy3) were captured on a PEG-streptavidin coated microscope slide using complementary capture oligonucleotides. For this, the slide was first incubated with 10 nM biotin-

modified complementary DNA oligoucleotide (5'-biotin-TTTTTGGAGGGAGGG) for 3 min, followed by 10 min incubation with 20-50 pM protein sample in 1×TAE-Mg buffer. After flushing out the excess protein, a movie was recorded under 532 nm illumination to locate Cy3 (~protein) molecules followed by the photobleaching of the fluorophores. A series of movies were recorded on the same field of view after injecting a substrate solution (Table S10†) supplemented with 3 mM NAD^+ and a variable concentration of resazurin (Fig. S28†). For each resazurin concentration, the average intensity of the spikes above the threshold was compared (Fig. S27†). While the fraction of molecules with spikes increases with the increase in resazurin concentration, the average intensity does not change with the resazurin concentration, suggesting that each spike corresponds to a single substrate turnover.[30]

Spike train analysis. Spike train analysis was carried out using a modified Rank Surprise (RS) method[31]. Briefly, inter-spike intervals (ISIs) were determined by calculating the time in between individual fluorescent spikes (Fig. S27†) for each molecule. The RS method was used to demarcate the start and end points of bursts after collecting ISIs for all molecules. A maximum expected ISI length of 5 s was used as a threshold to be included in a burst (Fig. S29†). Any sporadically appearing spikes outside a burst event are considered to be non-bursts.

Conclusions

In summary, we have used quantitative single molecule characterization and MD simulations to examine the sequence-level origins of sub-optimal performance of DNA-actuated enzyme nanoreactors. We discovered several specific yet generalizable features of the original sequence design that resulted in sub-optimal tweezer performance. Introducing a structure-guided rational design strategy, we were able to systematically eliminate each of these defects by implementing modifications for both the actuator and structural HJ elements. Our novel single molecule enzyme assay confirmed two specific,

independent pathways to increased activity of the tweezer-actuated enzyme nanoreactor in response to our design improvements that resulted in proper closure and elimination of heterogeneity among individual nanodevices. Because the design features identified here are general to many other DNA nanostructures, our work establishes guidelines for rationally improving the performance of nanodevices including reactors, chemical and biological sensors, as well as programmable nanomaterials.

Acknowledgements

The authors are grateful to Adam Krieger for contributions to the single molecule enzyme assays and to Mario Blanco and Xi Yu for their help with writing MATLAB scripts to analyze the same. This work was supported by Army Research Office MURI award W911NF-12-1-0420 to N.G.W., M.B. and H.Y.

References

1 N. Michelotti, A. Johnson-Buck, A. J. Manzo and N. G. Walter, *WIREs Nanomed. Nanobi.,* 2012, **4**, 139-152.
2 J. Fu, M. Liu, Y. Liu and H. Yan, *Acc. Chem. Res.,* 2012, **45**, 1215-1226.
3 A. V. Pinheiro, D. Han, W. M. Shih and H. Yan, *Nat. Nanotech.,* 2011, **6**, 763-772.
4 Y. Krishnan and M. Bathe, *Trends Cell Biol.,* 2012, **22**, 624-633.
5 D. Y. Zhang and G. Seelig, *Nat. Chem.,* 2011, **3**, 103-113.
6 N. C. Seeman, *Trends Biochem. Sci.,* 2005, **30**, 119-125.
7 J. Bath and A. J. Turberfield, *Nat. Nanotech.,* 2007, **2**, 275-284.
8 Y. He and D. R. Liu, *Nat. Nanotech.,* 2010, **5**, 778-782.
9 C. B. Rosen, L. B. KodalAnne, J. S. Nielsen, D. H. Schaffert, C. Scavenius, A. H. Okholm, N. V. Voigt, J. J. Enghild, J. Kjems, T. Tørring and K. V. Gothelf, *Nat. Chem.,* 2014, **6**, 804-809.
10 B. Yurke, A. J. Turberfield, A. P. Mills, Jr., F. C. Simmel and J. L. Neumann, *Nature,* 2000, **406**, 605-608.
11 R. Chhabra, J. Sharma, Y. Liu and H. Yan, *Nano Lett.,* 2006, **6**, 978-983.
12 S. Modi, G. S. M, D. Goswami, G. D. Gupta, S. Mayor and Y. Krishnan, *Nat. Nanotech.,* 2009, **4**, 325-330.
13 C. Zhou, Z. Yang and D. Liu, *J. Am. Chem. Soc.,* 2012, **134**, 1416-1418.
14 M. Liu, J. Fu, C. Hejesen, Y. Yang, N. W. Woodbury, K. Gothelf, Y. Liu and H. Yan, *Nat. Commun.,* 2013, **4**, 2127.
15 Y. Ke, G. Bellot, N. V. Voigt, E. Fradkov and W. M. Shih, *Chem. Sci.,* 2012, **3**, 2587-2597.
16 L. Mallik, S. Dhakal, J. Nichols, J. Mahoney, A. M. Dosey, S. Jiang, R. K. Sunahara, G. Skiniotis and N. G. Walter, *ACS Nano,* 2015, **9**, 7133-7141.
17 K. E. Dunn, F. Dannenberg, T. E. Ouldridge, M. Kwiatkowska, A. J. Turberfield and J. Bath, *Nature,* 2015, **525**, 82-86.
18 D. Rueda and N. G. Walter, *J. Nanosci. Nanotech.,* 2005, **5**, 1990-2000.
19 J. R. Widom, S. Dhakal, L. A. Heinicke and N. G. Walter, *Arch. Toxicol.,* 2014, **88**, 1965-1985.
20 A. Johnson-Buck, J. Nangreave, D. N. Kim, M. Bathe, H. Yan and N. G. Walter, *Nano Lett.,* 2013, **13**, 728-733.
21 P. W. K. Rothemund, *Nature,* 2006, **440**, 297-302.
22 Y. Ke, S. M. Douglas, M. Liu, J. Sharma, A. Cheng, A. Leung, Y. Liu, W. M. Shih and H. Yan, *J. Am. Chem. Soc.,* 2009, **131**, 15903-15908.
23 B. Wei, M. Dai, C. Myhrvold, Y. Ke, R. Jungmann and P. Yin, *J. Am. Chem. Soc.,* 2013, **135**, 18080-18088.
24 S. M. Miick, R. S. Fee, D. P. Millar and W. J. Chazin, *Proc. Natl. Acad. Sci.,* 1997, **94**, 9080-9084.
25 C. Hyeon, J. Lee, J. Yoon, S. Hohng and D. Thirumalai, *Nat. Chem.,* 2012, **4**, 907-914.
26 C. Joo, S. A. McKinney, D. M. J. Lilley and T. Ha, *J. Mol. Biol.,* 2004, **341**, 739-751.
27 C. Altona, *J. Mol. Biol.,* 1996, **263**, 568-581.
28 N. Nguyen, J. J. Birktoft, R. Sha, T. Wang, J. Zheng, P. E. Constantinou, S. L. Ginell, Y. Chen, C. Mao and N. C. Seeman, *J. Mol. Recognit.,* 2012, **25**, 234-237.
29 B. F. Eichman, J. M. Vargason, B. H. M. Mooers and P. S. Ho, *Proc. Natl. Acad. Sci.,* 2000, **97**, 3971-3976.
30 B. P. English, W. Min, A. M. van Oijen, K. T. Lee, G. Luo, H. Sun, B. J. Cherayil, S. C. Kou and X. S. Xie, *Nat. Chem. Biol.,* 2006, **2**, 87-94.
31 B. Gourévitch and J. J. Eggermont, *J. Neurosci. Methods,* 2007, **160**, 349-358.

32 G. G. Hammes, S. J. Benkovic and S. Hammes-Schiffer, *Biochemistry,* 2011, **50**, 10422-10430.
33 B. Liu, R. J. Baskin and S. C. Kowalczykowski, *Nature,* 2013, **500**, 482-485.
34 J. Fu, Y. R. Yang, A. Johnson-Buck, M. Liu, Y. Liu, N. G. Walter, N. W. Woodbury and H. Yan, *Nat. Nanotech.,* 2014, **9**, 531-536.
35 J. Abelson, M. Blanco, M. A. Ditzler, F. Fuller, P. Aravamudhan, M. Wood, T. Villa, D. E. Ryan, J. A. Pleiss, C. Maeder, C. Guthrie and N. G. Walter, *Nat. Struct. Mol. Biol.,* 2010, **17**, 504-512.
36 S. H. Chung and R. A. Kennedy, *J. Neurosci. Methods,* 1991, **40**, 71-86.
37 G. Haran, *Chem. Phys.,* 2004, **307**, 137-145.
38 S. M. Douglas, A. H. Marblestone, S. Teerapittayanon, A. Vazquez, G. M. Church and W. M. Shih, *Nucleic Acids Res.,* 2009, **37**, 5001-5006.
39 D.-N. Kim, F. Kilchherr, H. Dietz and M. Bathe, *Nucleic Acids Res.,* 2012, **40**, 2862-2868.
40 C. E. Castro, F. Kilchherr, D.-N. Kim, E. L. Shiao, T. Wauer, P. Wortmann, M. Bathe and H. Dietz, *Nat. Methods,* 2011, **8**, 221-229.
41 K. Pan, D.-N. Kim, F. Zhang, M. R. Adendorff, H. Yan and M. Bathe, *Nat. Commun.,* 2014, **5**, DOI: 10.1038/ncomms6578.
42 Accelrys Software Inc., San Diego, **2013**.
43 W. L. Jorgensen, J. Chandrasekhar, J. D. Madura, R. W. Impey and M. L. Klein, *J. Chem. Phys.,* 1983, **79**, 926-935.
44 J. C. Phillips, R. Braun, W. Wang, J. Gumbart, E. Tajkhorshid, E. Villa, C. Chipot, R. D. Skeel, L. Kalé and K. Schulten, *J. Comput. Chem.,* 2005, **26**, 1781-1802.
45 N. Foloppe and J. A. D. MacKerell, *J. Comput. Chem.,* 2000, **21**, 86-104.
46 A. D. MacKerell and N. K. Banavali, *J. Comput. Chem.,* 2000, **21**, 105-120.
47 O. Allnér, L. Nilsson and A. Villa, *J. Chem.Theory Comput.,* 2012, **8**, 1493-1502.
48 P. F. Batcho, D. A. Case and T. Schlick, *J. Chem. Phys.,* 2001, **115**, 4003-4018.
49 G. J. Martyna, D. J. Tobias and M. L. Klein, *J. Chem. Phys.,* 1994, **101**, 4177-4189.
50 S. E. Feller, Y. Zhang, R. W. Pastor and B. R. Brooks, *J. Chem. Phys.,* 1995, **103**, 4613-4621.
51 A. T. Brunger, in *X-PLOR, Version 3.1, Department of Molecular Biophysics and Biochemistry, Howard Hughes Medical Institute, Yale University, CT*, **1992**.
52 A. Bakan, L. M. Meireles and I. Bahar, *Bioinformatics,* 2011, **27**, 1575-1577.
53 F. Pedregosa, Varoquaux, G., Gramfort, A., Michel, V., Thirion, B., Grisel, O., Blondel, M., Prettenhofer, P., Weiss, R., Dubourg, V., Vanderplas, J., Passos, A., Cournapeau, D., Brucher, M., Perrot, M., Duchesnay, E. , *J. Mach. Learn. Res.,* 2011, 2825-2830.
54 J. Watson, F. A. Hays and P. S. Ho, *Nucleic Acids Res.,* 2004, **32**, 3017-3027.
55 R. Lavery, M. Moakher, J. H. Maddocks, D. Petkeviciute and K. Zakrzewska, *Nucleic Acids Res.,* 2009, **37**, 5917-5929.
56 M. J. B. Pereira, E. N. Nikolova, S. L. Hiley, D. Jaikaran, R. A. Collins and N. G. Walter, *J. Mol. Biol.,* 2008, **382**, 496-509.
57 R. Krishnan, M. R. Blanco, M. L. Kahlscheuer, J. Abelson, C. Guthrie and N. G. Walter, *Nat. Struct. Mol. Biol.,* 2013, **20**, 1450-1457.
58 P. Gonzalez-Tello, F. Camacho and G. Blazquez, *J. Chem. Eng. Data,* 1994, **39**, 611-614.
59 J. T. Edward, *J. Chem. Edu.,* 1970, **47**, 261.
60 A. Korosi and B. M. Fabuss, *Anal. Chem.,* 1968, **40**, 157-162.